Acta Cryst C STRUCTURAL CHEMISTRY

ISSN 2053-2296

The synthesis and crystal structure of (*E*)-2-{[(4-methoxynaphthalen-1-yl)methylidene]-amino}-4-methylphenol: Hirshfeld surface analysis, DFT calculations and anticorrosion studies

Ahmed Abderrahim Yahiaoui,[a] Nadir Ghichi,[b]* Douniazed Hannachi,[c,d] Bilel Mezhoud,[b,e] Amel Djedouani,[f,g] Khairedine Kraim,[a] Aurélien Crochet[h] and Helen Stoeckli-Evans[i]

[a]Higher Normal School of Technological Education of Skikda (ENSET), Algeria, [b]Unit of Research CHEMS, Chemistry Department, University of Mentouri Brothers, Constantine 1, Algeria, [c]Laboratory of Electrochemistry, Molecular Engineering and Redox Catalysis (LEIMCR), Department of Basic Education in Technology, Faculty of Technology, University Ferhat Abbas, Setif-1, Algeria, [d]Department of Chemistry, Faculty of Sciences, University of Setif-1, Setif, Algeria, [e]Faculty of Exact Sciences and Computer Science, University of Jijel, BP 98, Jijel 18000, Algeria, [f]Laboratory of Analytical Physicochemistry and Crystallochemistry of Organometallic and Biomolecular Materials, University of Constantine 1, 25000, Algeria, [g]Superior Normal School of Constantine, University of Constantine 3, 25000, Algeria, [h]Chemistry Department, University of Fribourg, Chemin du Musée 9, CH-1700 Fribourg, Switzerland, and [i]Institute of Physics, University of Neuchâtel, rue Emile-Argand 11, 2000 Neuchâtel, Switzerland. *Correspondence e-mail: nadirghichi@yahoo.com

Received 21 May 2023
Accepted 3 July 2023

Edited by M. Rosales-Hoz, Cinvestav, Mexico

This article is part of a collection of articles to commemorate the founding of the African Crystallographic Association and the 75th anniversary of the IUCr.

Keywords: Schiff base; crystal structure; Hirshfeld surface analysis; anticorrosion; DFT calculations; carbaldehyde; quantum chemical calculations.

CCDC reference: 2279139

Supporting information: this article has supporting information at journals.iucr.org/c

The title Schiff base compound, (*E*)-2-{[(4-methoxynaphthalen-1-yl)methylidene]amino}-4-methylphenol, $C_{19}H_{17}NO_2$ (**I**), was synthesized *via* the reaction of 2-amino-4-methylphenol with 4-methoxynaphthalene-1-carbaldehyde. The structure of **I** was characterized by NMR, IR and UV–Vis spectroscopies in different solvents. The interatomic contacts in the crystal structure were explored using Hirshfeld surface analysis, which, together with the two-dimensional fingerprint plots, confirm the predominance of dispersion forces in the crystal structure. The molecule of **I** has a twisted conformation, with the mean plane of the naphthalene ring system being inclined to the plane of the phenol ring by 33.41 (4)°. In the crystal, molecules are linked by C—H···O hydrogen bonds to form inversion dimers. There are parallel-displaced π–π interactions present, together with C—H···π interactions, resulting in the formation of a three-dimensional structure. The anticorrosion potential of **I** was also investigated using density functional theory (DFT) in the gas phase and in various solvents. The compound was shown to exhibit significant anticorrosion properties for iron and copper. The molecular structure of **I** was determined by DFT calculations at the M062X/6-311+g(d) level of theory and compared with the crystallographically determined structure. Local and global reactivity descriptors were computed to predict the reactivity of **I**. Excellent agreement was observed between the calculated results and the experimental data.

1. Introduction

Schiff bases, also known as imines, are organic compounds containing an azomethine functional group (>C═N–). They are formed by the condensation reaction of derivatives of a primary amine (NH_2) and a carbonyl compound (C═O), such as an aldehyde or a ketone (Yakan *et al.*, 2023). The first Schiff base compounds were synthesized by the Italian scientist Hugo Schiff in 1864 (Qin *et al.*, 2013). They are characterized by the chemical diversity of their structures, *i.e.* $R_1R_2C{=}NR_3$, with R_1 and R_2 indicating organic side chains, while R_3, bound to the N atom, may be an aryl or alkyl group. Due to their interesting and important properties, many researchers have explored ways to obtain general, simple, efficient and inex-

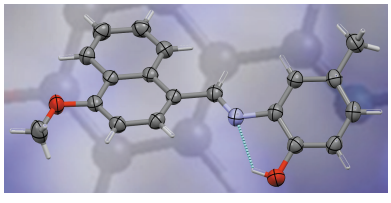

pensive methods for synthesizing Schiff bases. At present, several chemical procedures exist for preparing these compounds, including gentle synthetic methods, such as reflux (Brown & Granneman, 1975; Li *et al.*, 2016; Olar *et al.*, 2017) or microwave-assisted synthesis (Segura *et al.*, 2016; Sk *et al.*, 2020; Mishra *et al.*, 2020). Schiff bases are of great importance in organic chemistry due to their chemical properties and they have wide-ranging applications. They are also used as ligands in coordination chemistry (Mohamed, 2006; Tarafder *et al.*, 2000; Chandra *et al.*, 2009), as intermediates in organic synthesis (Matsumoto *et al.*, 2020) and as colorimetric indicators in mineral analysis.

Recent research has been focused on studying the effect of corrosion on metals and alloys, and developing materials and techniques to prevent it (John *et al.*, 2023). Corrosion prevention relies mainly on the physical and chemical properties of the inhibitor molecule, the π-orbital properties of the electron donor and the electronic structure of the inhibitor (Obot *et al.*, 2009). One effective way of preventing corrosion is the use of organic inhibitors (Zheludkevich *et al.*, 2005; Aljourani *et al.*, 2009). Schiff bases can be used to reduce corrosion and minimize negative environmental effects, based on the ease of their synthesis from relatively inexpensive starting materials and their environmentally friendly properties (Lashgari *et al.*, 2010; Küstü *et al.*, 2007). It is well known that the behaviour of the inhibitors depends on the interaction between the functional groups in the molecule and the surfaces of the metal. The ability of Schiff bases to form closely packed stable complexes in the field of metal ion coordination classifies them as compounds capable of preventing corrosion. The Schiff base is adsorbed onto the metal surface due to the presence of lone-pair electrons on the N atom in the –CH═N– group and the distribution of π double-bond electrons in the structure. This adsorption behaviour leads to the formation of a very thin layer that covers the surface of the metal, thus preventing corrosion (Afshari *et al.*, 2023; Zhang *et al.*, 2023; Jafari *et al.*, 2022).

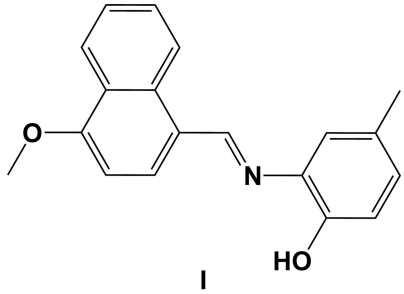

I

Scheme 1

In view of this interest, we report herein on the synthesis of the title compound, namely, (*E*)-2-{[(4-methoxynaphthalen-1-yl)methylidene]amino}-4-methylphenol (**I**). The structure of **I** was fully characterized by crystallographic and spectroscopic techniques. The anticorrosion efficiency of **I** was evaluated. Quantum chemical calculations were also carried out for the estimation of the geometrical parameters and reactivity indices of **I**.

2. Experimental

2.1. Measurements and materials

The reagents used for the synthesis of compound **I** were obtained commercially and were used without further purification. The NMR spectra were recorded on an RMN 400 MHz Bruker Ascend for ^{1}H. IR spectra were recorded on a Shimadzu IRAffinity-1S spectrometer. The UV–Vis spectra were recorded from 200 to 600 nm using a Unicam Helios Alpha spectrophotometer, with a quartz cell having a path length of 1 cm.

2.2. Anticorrosion experiment

The synthesized compound was subjected to an evaluation of its corrosion-inhibiting efficiency of a steel in sulfuric acid medium, using polarization curves and electrochemical impedance spectroscopy (EIS).

For the experimental conditions, the electrochemical tests were performed in a conventional three-electrode Pyrex glass cell with a capacity of 20 ml using a Gamry Instruments potentiostat/galvanostat/ZRA (Reference 3000), controlled by Gamry framework analysis software (*Gamry Echem Analyst*, https://www.gamry.com/support-2/software/). The exposed surface area of the working electrode (steel) was 0.18 cm^2. Before each test, the working electrode was polished mechanically using emery paper of decreasing grain size (400, 600, 1200 and 2000) under a water jet, then degreased with ethanol, washed with double-distilled water and air-dried. A platinum electrode was used as a counter-electrode (auxiliary electrode), its role being to ensure the passage of electric current in the electrochemical cell. A saturated calomel electrode [Hg/Hg_2Cl_2/KCl(sat)/ECS] was used as the reference electrode.

Polarization curves are plotted in a potential range from −800 to −200 mV at a scan rate of 1 mV s^{-1}. The impedance measurements were carried out at open-circuit potential (Eocp) using ac signals of 10 mV amplitude (peak to peak) at frequencies between 100 kHz and 0.01 Hz (Mezhoud *et al.*, 2016; Sakki *et al.*, 2022).

2.3. Computational details

Density functional theory (DFT) calculations were performed for **I** in the gas phase and in various solvents [*n*-hexane, chloroform, acetone, methanol, dichloromethane (DCM) and water]. All calculations were carried out using *GAUSSIAN16* software (Frisch *et al.*, 2019) without any restriction on the symmetry. The geometry optimization, harmonic frequency calculations and reactivity descriptors were carried out and generated at the M06-2X/6-311+G(d) level of theory. For the solvent-phase calculations, the default self-consistent (solvent) reaction field in *GAUSSIAN16* was used, which is the polarizable continuum model (PCM) using the integral equation formalism variant (IEFPCM).

Electronic chemical potential (μ) is the tendency of an atom or molecule to attract electrons; it is given by Equation (1)

(see the supporting information for all equations and relations).

The chemical hardness (η) expresses the resistance of a system to change its number of electrons; it is calculated with relation 2.

The global electrophilicity index (ω), introduced by Parr *et al.* (1999), is calculated from the hardness and chemical potential [see Equation (3)].

During the interaction between two molecular systems, the electrons flow from the lower electronegativity (nucleophile, Nu) to the higher electronegativity (electrophile, E) until the chemical potential becomes equalized. The fraction of the transferred electron, ΔN [see Equation (4)], was estimated according to Pearson (Parr & Pearson, 1983; Hannachi *et al.*, 2015; Fellahi *et al.*, 2021).

On the other hand, the Fukui function $f(r)$ and the dual descriptor $\Delta f(r)$ are local reactivity descriptors which reflect the ability of a compound site to donate or accept electrons. The Fukui function proposed by Parr & Yang (1984) can be evaluated for nucleophilic attack f_k^+, electrophilic attack f_k^- and radical (neutral) attack f_k^0 (see Equations 5, 6 and 7).

Furthermore, the local philicity index (ω_k^α) can easily be evaluated from Equations (8) and (9).

The dual descriptor $\Delta f(r)$ (Morell *et al.*, 2005; Roy *et al.*, 1998) is more convenient to use than the Fukui function (Chen *et al.*, 2022).

2.4. Synthesis and crystallization

A mixture of 2-amino-4-methylphenol (0.246 g) and 4-methoxynaphthalene-1-carbaldehyde (0.372 g) in methanol (25 ml) was stirred for 1 h. At the end of the reaction, the solvent was evaporated *in vacuo*. The resulting residue was recrystallized from methanol to give small orange block-like crystals (m.p. 147–149 °C).

2.5. Refinement

Crystal data, data collection and structure refinement details are summarized in Table 1. The OH H atom of **I** was located in a difference Fourier map and refined freely. The C-bound H atoms were positioned geometrically (C—H = 0.94–0.97 Å) and refined as riding, with $U_{iso}(H) = 1.5U_{eq}(C)$ for methyl H atoms and $1.2U_{eq}(C)$ otherwise.

Table 1
Experimental details.

Crystal data	
Chemical formula	$C_{19}H_{17}NO_2$
M_r	291.33
Crystal system, space group	Triclinic, $P\overline{1}$
Temperature (K)	250
a, b, c (Å)	7.7740 (4), 7.9955 (4), 12.4836 (6)
α, β, γ (°)	106.383 (4), 98.191 (4), 93.279 (4)
V (Å^3)	732.96 (7)
Z	2
Radiation type	Mo $K\alpha$
μ (mm^{-1})	0.09
Crystal size (mm)	0.61 × 0.39 × 0.18
Data collection	
Diffractometer	STOE IPDS II
Absorption correction	Multi-scan (*MULABS*; Spek, 2020)
T_{min}, T_{max}	0.875, 1.000
No. of measured, independent and observed [$I > 2\sigma(I)$] reflections	11018, 3090, 2742
R_{int}	0.018
$(\sin\theta/\lambda)_{max}$ (Å^{-1})	0.634
Refinement	
$R[F^2 > 2\sigma(F^2)]$, $wR(F^2)$, S	0.038, 0.113, 1.04
No. of reflections	3090
No. of parameters	205
H-atom treatment	H atoms treated by a mixture of independent and constrained refinement
$\Delta\rho_{max}$, $\Delta\rho_{min}$ (e Å^{-3})	0.20, −0.14

Computer programs: *WinXpose*, *Recipe*, *Integrate* and *LANA* in *X-AREA* (Stoe & Cie, 2022), *SHELXS97* (Sheldrick, 2008), *PLATON* (Spek, 2020), *Mercury* (Macrae *et al.*, 2020), *SHELXL2018* (Sheldrick, 2015) and *publCIF* (Westrip, 2010).

3. Results and discussion

3.1. Analytical data

3.1.1. IR spectroscopy. In the experimental IR spectrum of **I**, the C—H_{ar} (ar is aromatic) band at 2931–2846 cm^{-1}, the C═C elongation bands at 1512 cm^{-1} and the deformation domain in the C—H_{ar} plane (1000 to 700 cm^{-1}) were of particularly high intensity. The C—H_{ar} region can be divided into three subregions: adjacent 1H (1022 to 906 cm^{-1}), adjacent 2H (centred on 819 cm^{-1}) and 4H (centred on 750 cm^{-1}). The IR spectra show the main characteristic imine (C═N) band at 1568 cm^{-1}. A band located at 3348 cm^{-1} can be attributed to the stretching of the hydroxy function (–OH) of the phenol group. The peak obtained at an average intensity of 1512 cm^{-1} can be attributed to the elongation vibration of the C═C aromatic bond. The observed strong peak at 1217 cm^{-1} can be attributed to the stretching of the C—O—C bond of the methoxy ether group (–OCH_3) present in the molecule, and the strong peak at 1093 cm^{-1} can be attributed to the stretching of the C—OH bond in the ring. The band observed around 1350 cm^{-1} was assigned to CH_3 bending. The IR spectra of **I** are consistent with the structure determined by X-ray diffraction analysis, indicating a high degree of agreement between the two methods.

3.1.2. ^{1}H NMR spectroscopy. Compound **I** was characterized by its ^{1}H NMR spectrum, which exhibited several diagnostic signals. ^{1}H NMR (400 MHz, $CDCl_3$): δ 2.34 (3H, *s*, CH_3), 4.06 (3H, *s*, OCH_3), 6.93–6.88 (2H, *m*, H17, H3), 6.99 (1H, *dd*, J = 8.2, 1.5 Hz, H16), 7.11 (1H, *s*, H14), 7.55 (1H, *ddd*, J = 8.1, 6.9, 1.0 Hz, H6), 7.64 (1H, *ddd*, J = 8.4, 6.9, 1.3 Hz, H7), 8.07 (1H, *d*, J = 8.2 Hz, H8), 8.35 (1H, *d*, J = 7.7 Hz, H2), 8.96 (1H, *d*, J = 8.5 Hz, H5), 9.17 (1H, *s*, CHN).

For the ^{1}H NMR spectrum of **I** (see Figs. S9 and 10 in the supporting information), two singlets were observed at δ = 2.34 and 4.06 ppm, corresponding to the protons of methyl groups 19 and 11, respectively. Protons H17 and H3 were observed in the 6.93–6.88 ppm region and exhibit a multiplet pattern. There is a 1H integration doublet of doublets at δ = 6.99 ppm, with coupling constants J = 8.2 and 1.5 Hz, which is characteristic for proton H16. The singlet with a 1H integration at δ = 7.11 ppm was assigned to proton H14. Two 1H

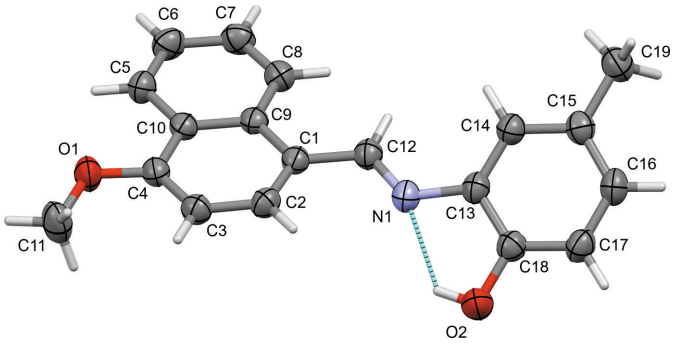

Figure 1
A view of the molecular structure of **I**, with the atom labelling. The displacement ellipsoids are drawn at the 50% probability level and the intramolecular O—H···N hydrogen bond is shown as a dashed line.

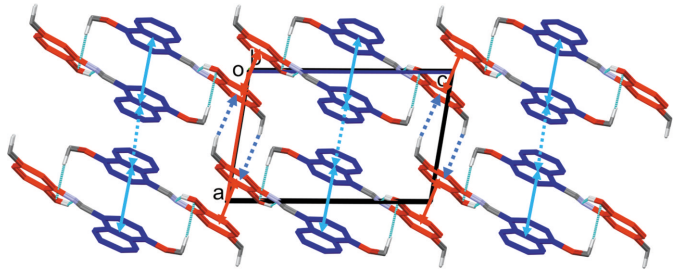

Figure 2
A view along the *b* axis of the crystal packing of **I**. The intramolecular O—H···N and intermolecular C—H···O hydrogen bonds are shown as dashed lines, and the C—H···π interactions as blue dashed arrows (see Table 2). The coloured double-headed arrows indicate the presence of π–π interactions (naphthalene rings are shown in blue and phenol rings in red). Only the H atoms involved in these interactions have been included.

integrations as doublet of doublet of doublets were detected at δ = 7.55 and 7.64 ppm, with coupling constants J = 8.1/6.9/1.0 and 8.4/6.9/1.3 Hz, respectively, which is characteristic for protons H6 and H7, respectively. Three 1H integration doublets were detected at δ = 8.07, 8.35 and 8.69 ppm, with coupling constants J = 8.2, 7.7 and 8.5 Hz, respectively, which is characteristic of an *ortho* coupling for protons H8, H2 and H5, respectively. Finally, a 1H integration singlet was detected at δ = 9.17 ppm, corresponding to the proton of the CH═N group.

3.2. Crystallographic studies

3.2.1. Molecular and crystal structure. The molecular structure of **I** is illustrated in Fig. 1. A search of the Cambridge Structural Database (CSD, Version 5.43, last update November 2022; Groom *et al.*, 2016) returned only one similar compound, *viz*. 5-methyl-2-[(naphthalen-1-ylmethylidene)amino]-phenol (CSD refcode EXIPIL; Orona *et al.*, 2011).

In **I**, the mean plane of the naphthalene ring system (atoms C1–C10; r.m.s. deviation 0.015 Å) is inclined to the plane of the phenol ring (C13–C18) by 33.41 (4)°. In EXIPIL, the corresponding dihedral angle is only 7.96 (9)°. The methoxy group in **I** lies slightly out of the plane of the ring to which it is attached, with the dihedral angle of $CH_3—O—C_{ar}$ with respect to the naphthalene ring plane (C1–C4/C9/C10) being 6.08 (12)°. There is an intramolecular hydrogen bond (O2—H2O···N1) involving the phenol –OH group and the amino N atom (Table 2), forming an *S*(5) ring motif. The configuration about the C═N double bond is *E* and the C12═N1 bond length is 1.2741 (14) Å. This configuration is the same as in EXIPIL, where the C═N bond length is 1.273 (3) Å.

In the crystal of **I**, molecules are linked by C—H···O hydrogen bonds to form inversion dimers (Fig. 2 and Table 2). As shown in Fig. 2, the dimers are linked by parallel-displaced π–π interactions involving inversion-related naphthalene rings [blue; the centroid–centroid distance is 3.967 (1) Å, the interplanar distance is 3.4707 (4) Å and the slippage is 1.922 Å] and inversion-related phenol rings [red; the centroid–centroid distance is 3.732 (1) Å, the interplanar distance is 3.445 (1) Å and the slippage is 1.437 Å], forming slabs lying

Table 2
Hydrogen-bond geometry (Å, °).

*Cg*1 is the centroid of the phenol ring (atoms C13–C18).

D—H···*A*	*D*—H	H···*A*	*D*···*A*	*D*—H···*A*
O2—H2O···N1	0.84 (2)	2.069 (18)	2.6436 (13)	126 (2)
C11—H11*B*···O2^{i}	0.97	2.51	3.4725 (19)	170
C19—H19*A*···*Cg*1^{ii}	0.97	2.79	3.7362 (14)	165

Symmetry codes: (i) $-x, -y+2, -z+1$; (ii) $-x-1, -y+1, -z$.

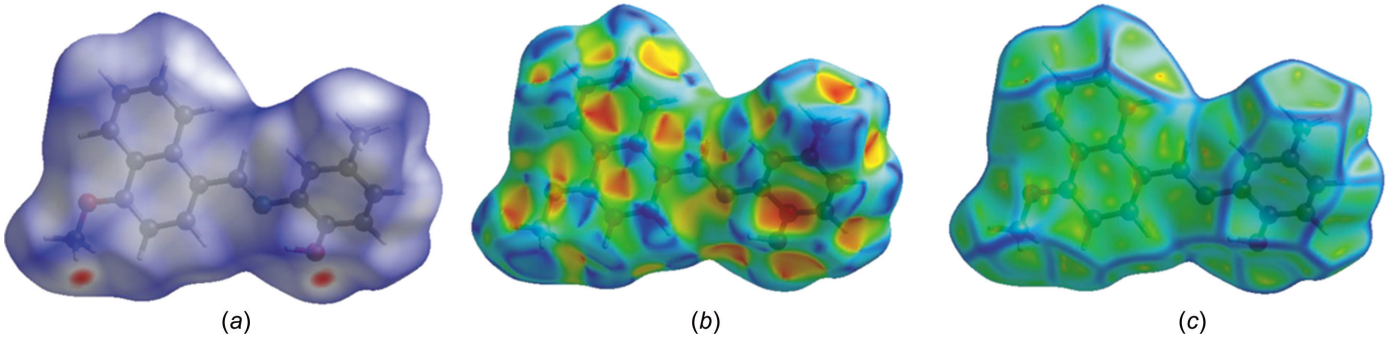

Figure 3
The Hirshfeld surface of compound **I** mapped over (*a*) d_{norm} in the colour range from −0.1552 to 1.2739 a.u., (*b*) the shape-index property and (*c*) the curvedness.

Table 3
Polarization curves and electrochemical impedance spectroscopy (EIS).

Method	Polarization curves				EIS	
	Concentration (*M*)	E_{corr} (mV)	I_{corr} (μA cm^{-2})	IE (%)	R_{ct} (Ω cm^2)	IE (%)
H_2SO_4	0.5	432	2794.44	–	8.08	–
Inhibitor **I**	5×10^{-3}	498	48.94	98.24	266.22	96.96

parallel to the *bc* plane. The slabs are linked by a C—H···π interaction (Table 2) and a second π–π interaction involving inversion-related naphthalene rings [blue; the centroid–centroid distance is 3.819 (1) Å, the interplanar distance is 3.5302 (4) Å and the slippage is 1.458 Å] to form a three-dimensional (3D) framework.

3.2.2. Hirshfeld surface analysis and two-dimensional (2D) fingerprint plots. The Hirshfeld surface analysis (Spackman & Jayatilaka, 2009) and the associated 2D fingerprint plots (McKinnon *et al.*, 2007) were performed and created with *CrystalExplorer21* (Spackman *et al.*, 2021), following the protocol of Tiekink and collaborators (Tan *et al.*, 2019).

The various Hirshfeld surfaces (HS) of **I** are shown in Fig. 3. There are important contacts present in the crystal; the stronger hydrogen bonds are indicated by the small and large red zones in Fig. 3(*a*). The presence of π–π interactions is confirmed by the blue and red triangular shapes in Fig. 3(*b*), and by the flat regions around the naphthalene and phenol rings in Fig. 3(*c*).

The 2D fingerprint plots for **I** are given in Fig. 4. They reveal that the principal contributions to the overall HS surface involve H···H contacts at 54.9% and C···H/H···C contacts at 19.1%. The latter are the result of the C—H···π interactions in the crystal. These are followed by the O···H/H···O and C···C contacts at 11.1% each. These are related to the C—H···O hydrogen bonds and the various π–π interactions present in the crystal (see Table 2 and Fig. 3). The N···H/H···N contacts at 2.7% reflect the presence of an intramolecular O—H···N hydrogen bond. The O···C/C···O and N···C/C···N contacts amount to only 0.6 and 0.5%, respectively.

3.2.3. Energy frameworks. Fig. 5 shows a comparison of the energy frameworks calculated for **I**, including the electrostatic potential forces (E_{ele}), the dispersion forces (E_{dis}) and the total energy diagrams (E_{tot}). The energies were obtained using the wavefunction at the HF/3-2IG level of theory. The cylindrical radii are proportional to the relative strengths of the corresponding energies (Spackman *et al.*, 2021; Tan *et al.*, 2019). They have been adjusted to the same scale factor of 90 with a cutoff value of 6 kJ mol^{-1} within a radius of 6 Å of a central reference molecule. As can be seen in Fig. S1 (see supporting information), the interatomic interactions in the crystal are dominated by dispersion forces (E_{dis}), reflecting the absence of classical intermolecular hydrogen bonds in the crystal. The colour-coded interaction mappings within a radius of 6 Å of a central reference molecule and the various contributions to the total energy (E_{tot}) for **I** are given in Fig. S1.

3.3. Anticorrosion study

The polarization curves and electrochemical impedance spectroscopy (EIS) plots of steel in 0.5 *M* H_2SO_4 medium in the absence and presence of the inhibitor **I** are presented in

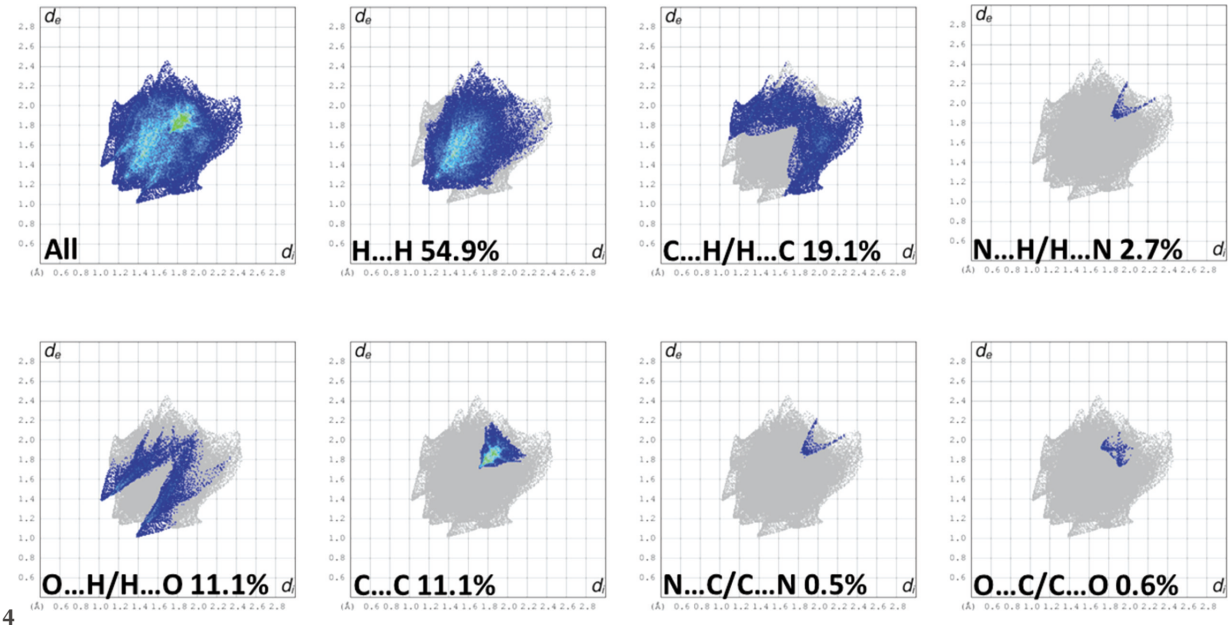

Figure 4
The full 2D fingerprint plots for compound **I** and those delineated into H···H, C···H/H···C, N···H/H···N, O···H/H···O, C···C, N···C/C···N and O···C/C···O contacts.

Table 4
Structural parameters (Å, °) calculated in the gas phase and different solvents using the M062x/6-311+g(d) level of theory.

	Exp.	Gas (ε = 1)	*n*-Hexane (ε = 1.8819)	Chloroform (ε = 4.711)	DCM (ε = 8.93)	Acetone (ε = 20.493)	Methanol (ε = 32.613)	Water (ε = 78.355)
C27—N4	1.410	1.406	1.406	1.406	1.407	1.407	1.407	1.407
N4—C25	1.274	1.275	1.276	1.277	1.277	1.277	1.277	1.277
C25—C5	1.460	1.466	1.466	1.466	1.466	1.466	1.466	1.465
C35—O2	1.370	1.352	1.354	1.356	1.357	1.357	1.358	1.358
O1—C10	1.360	1.350	1.348	1.347	1.346	1.346	1.346	1.346
O2—H3	2.066	2.124	2.125	2.124	2.124	2.123	2.122	2.122
C27—N4—C25	120	120	120	120	120	120	120	120
N4—C25—C5	122	122	122	122	122	122	120	120
C27—N4—C25—C5	178	175	175	175	175	176	176	176
R.m.s. error (RMSE) (Å)	–	0.368	0.353	0.340	0.335	0.330	0.329	0.328

Figs. 6 and 7, respectively. It can be seen that in the presence of 5×10^{-3} *M* of **I**, the anodic and cathodic curve shifts towards the lower values of the current densities, which means that the addition of this compound to the corrosive medium reduces the anodic dissolution of the steel and also delays the reduction of hydrogen ions, which may be due to adsorption on the steel surface (Li *et al.*, 2011; Deng *et al.*, 2011). The diameter of the capacitive loop increases considerably after addition of the inhibitor, indicating the formation of an inhibition film on the steel surface.

The values of the electrochemical parameters and of the inhibitory efficiency (IE, %) in the absence and in the presence of 5×10^{-3} *M* of the inhibitor obtained by the polarization curves and the electrochemical impedance spectroscopy (EIS) are given in Table 3.

The IE was calculated using the following equations:

$$\text{IE}\ (\%) = I_{\text{corr}(0)} - I_{\text{corr}}/I_{\text{corr}(0)} \times 100 \qquad (1)$$

$$\text{IE}\ (\%) = R_{\text{ct}} - R_{\text{ct}(0)}/R_{\text{ct}} \times 100 \qquad (2)$$

where I_{corr} and $I_{\text{corr}(0)}$ are the corrosion current densities in the absence and presence of the inhibitor, respectively, and R_{ct} and $R_{\text{ct}(0)}$ are the charge-transfer resistance values with and without inhibitor.

From the parameters shown in Table 3, it can be seen that the addition of 5×10^{-3} *M* of compound **I** to the corrosive medium decreases significantly the value of the corrosion current density (I_{corr}) and increases the charge-transfer resistance. The decrease in I_{corr} and the increase in load-transfer resistance can be attributed to the adsorption of inhibitor molecules onto the steel surface, thus forming a protective layer. On the other hand, the value of the corrosion potential (E_{corr}) moves in a negative direction. This shift relative to H_2SO_4 alone is less than 85 mV/SCE (about 66 mV). This suggests that **I** acts as a mixed inhibitor (Musa *et al.*, 2010; Döner *et al.*, 2011). The IE values calculated by both methods

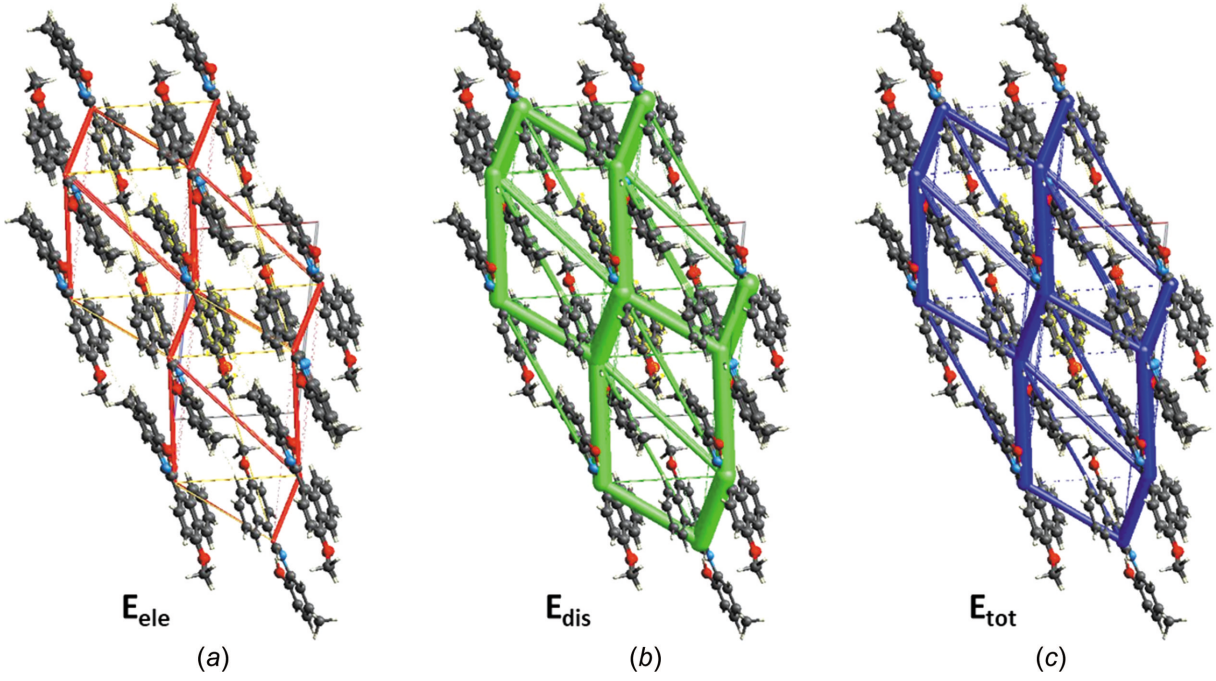

Figure 5
The energy frameworks calculated for **I** viewed along the *b*-axis direction, showing the electrostatic potential forces (E_{ele}, red), the dispersion forces (E_{dis}, green) and the total energy diagrams (E_{tot}, blue).

Table 5
Thermodynamic parameters calculated in the gas phase and different solvents at room temperature using the M062x/6-311+g(d) level of theory.

	Gas (ε = 0)	*n*-Hexane (ε = 1.8819)	Chloroform (ε = 4.711)	Acetone (ε = 20.493)	DCM (ε = 8.93)	Methanol (ε = 32.613)	Water (ε = 78.355)
H (a.u.)	−938.949911	−938.955536	−938.959863	−938.962279	–	−938.962556	−938.962832
G (a.u.)	−939.017972	−939.023693	−939.028201	−939.030818	–	−939.031122	−939.031430
C_v (cal mol^{-1} K^{-1})	73.813	73.916	74.012	74.076	–	74.084	74.092
S (cal mol^{-1} K^{-1})	143.245	143.448	143.828	144.252	–	144.309	144.376

show good protection of this compound against the corrosion of API 5L Grade B steel in 0.5 *M* sulfuric acid.

3.4. Experimental absorption spectral analysis

The absorption spectra of compound **I** in solvents of different polarities were measured in order to study the effects of solvent polarities on the electronic absorption spectra of the compound (see Fig. S2). A series of absorption spectra were recorded in *n*-hexane, chloroform, dichloromethane (DCM), acetone, methanol and water solutions (at concentrations of the order of 10^{-4} mol l^{-1}) to study the role of solvent polarity in modifying the electronic states of the compound (Fig. S2). Two main absorption bands characterize the absorption spectra of the studied compound; the first is attributed to the electronic transitions $\pi\rightarrow\pi^*$ and the second to the transition n$\rightarrow\pi^*$.

From the absorption spectra, we can see that the use of solvents of different polarities caused differences in the electronic transitions, which led to differences in the absorption spectra. Two main absorption bands characterize the different absorption spectra of our molecule. The first bands around 240 nm were very close to each other for all the solvents except acetone, where we observed a bathochromic shift.

In general, the presence of an enol–keto equilibrium, the nature of the substitutions, the solvent environment, hydrogen bonding, temperature, pH and changes in the dipole moment of the molecules are the key factors in determining the solvatochromism of compounds (Zakerhamidi *et al.*, 2012).

3.5. DFT and TD–DFT studies

3.5.1. DFT-optimized geometry. The geometry optimization of **I** was carried out using the X-ray coordinates and DFT calculations at the M062x/6-311+g(d) level in the gas phase and various solvent environments (see Fig. S3 in the supporting information). Table 4 includes the equilibrium bond distances and angles, as well as the r.m.s. error (RMSE) values.

The optimized structure of compound **I** compares well with the experimental data. In particular, the calculated C27—N4, C35—O2 and C10—O1 bond lengths in the gas phase and solvents are smaller than the experimental values (by approximately −0.003, −0.014 and −0.012 Å, respectively), whereas the N4—C25 and C25—C5 bonds are longer than the experimental values by *ca* 0.002 and 0.005 Å. Additionally, Fig. S5 presents an overlay of the X-ray crystallographic structure and the optimized geometry of **I** in water, and the RMSE values were calculated as 0.368, 0.353, 0.340, 0.329, 0.330 and 0.328 Å in the gas phase, *n*-hexane, chloroform, methanol, acetone and water, respectively. These results indicate that the RMSE values are lower in polar solvents (water, acetone and methanol) in comparison to nonpolar solvents. Based on these findings, we can deduce that the calculated geometries, which include bond lengths and angles, are in excellent agreement with the experimental data. On the other hand, it should be noted that the evaluation of the computed thermodynamic parameters at 298.15 K in Table 5 showed a minimal effect of the solvents on the enthalpy (H^o), Gibbs free energy (G^o) and the molar heat capacity (C_v) of the title compound.

3.5.2. Inhibition mechanism. To investigate the interaction between the inhibitor molecule and the bulk metal surface (Fe and Cu), we computed the global and local reactivity indices; they are listed in Table 6, and in Table S1 in the supporting information. Our quantum chemical calculations revealed that the gas phase exhibited the lowest values of chemical hardness, suggesting the weaker stability of **I**. Conversely, the solvent demonstrated the largest hardness value of **I** (greater stability). The order of increasing hardness in the studied compound was as follows: η(water) = η(acetone) = η(methanol) > η(DCM) > η(chloroform) > η(*n*-hexane). On the other hand, the chemical potential of **I** was found to be greater in the gas phase compared to that in the solvent (gas > *n*-hexane > chloroform > DCM > acetone > methanol > water). These outcomes suggest that the tendency of the electron to depart from the equilibrium inhibitor compound increases with a decrease in the dielectric constant (which increases from the gas to nonpolar and polar environments). In simpler terms, the increase in the μ values signifies that **I** has a greater inclination to donate electrons in *n*-hexane than in any other solvent. Based on the global electrophilicity scale (Hannachi *et al.*, 2015, 2021; Domingo *et al.*, 2002), inhibitor molecule **I** can be categorized as a strong electrophile, with values ranging from 1.446 to 1.55 eV.

Electronegativity (χ) is an excellent parameter that helps to determine the direction of electron flow between the metal surface and the inhibitor compound until a balance in chemical potential is achieved. When the inhibitor molecule is adsorbed on the metal surface, particularly on iron and copper with electronegativities of 7 and 4.9 eV (Michaelson, 1977; Lemoui *et al.*, 2023; Lesar & Milošev, 2009), respectively, electrons should move in the system from the less electronegative to the more electronegative element. Our calculations reveal that **I** exhibits less electronegativity than iron and copper, indicating that it is capable of transferring electrons to the metal surface and the inhibitor will thus exhibit better kinetic interaction with the iron surface compared to the copper surface (Lemoui *et al.*, 2023).

Table 6
Highest occupied molecular orbital (HOMO) energy (ε_{HOMO}, eV), chemical potential (μ, eV), chemical hardness (η, eV), global electrophilicity index (ω, eV) and fraction of the transferred electron (ΔN, eV).

	Gas	*n*-Hexane	Chloroform	DCM	Acetone	Methanol	Water
ε_{HOMO}	−6.806	−6.883	−6.941	−6.959	−6.971	−6.975	−6.978
μ	5.578	5.602	5.612	5.614	5.615	5.615	5.615
η	−4.016	−4.082	−4.134	−4.152	−4.164	−4.167	−4.170
ω	1.446	1.487	1.522	1.535	1.543	1.546	1.549
ΔN, **I**/Fe	0.267	0.260	0.255	0.253	0.252	0.252	0.251
ΔN, **I**/Cu	0.086	0.080	0.075	0.073	0.072	0.072	0.072

ΔN, the number of transferred electrons, is a useful quantum chemical descriptor for investigating and studying the interactions between a metal and an inhibitor. This descriptor can provide valuable insights into the mechanism of inhibition and help predict the inhibitory activity of new compounds. The results given in Table 6 revealed that the ΔN value of **I**/Fe was three times greater than that of **I**/Cu, suggesting a stronger interaction between the corrosion inhibitor and the iron surface in both the gas and the solvent phases compared to the interaction between the inhibitor and copper. Additionally, in gas and nonpolar media (*n*-hexane, chloroform and DCM), compound **I** exhibited a slightly higher ΔN value among the tested solvents, indicating a slightly greater potential for releasing electrons into the low-lying vacant *d* orbitals of the metal (Lemoui *et al.*, 2023; Alaoui Mrani *et al.*, 2021) relative to acetone, methanol and water. This observation suggests that compound **I** may be a promising inhibitor for preventing corrosion in non-aqueous environments and provides insight into the factors that contribute to its inhibitory activity. By understanding the electronic structure and the interaction of the inhibitor with the metal surface, we can develop new and more effective corrosion inhibitors for various industrial applications.

On the other hand, a corrosion inhibitor with weak electrophilicity (ω) exhibits a good potential for releasing electrons, which leads to efficient interaction and stabilization on metal surfaces. The trend of electrophilicity (ω) is as follows: water > methanol > acetone > DCM > chloroform > *n*-hexane > gas. The results indicate that gas, *n*-hexane, chloroform and DCM (nonpolar media) showed a smaller value of ω than the polar solvent, suggesting that these media contribute significantly to the corrosion inhibition potential.

The sites that exhibit the highest values of condensed Fukui functions (FFs) f^- and f^+ correspond to those suitable for electrophilic and nucleophilic attacks, respectively. Table 7 shows the values of the Fukui function and a dual descriptor for **I** after nucleophilic and electrophilic attack. DFT calculations show that the local reactivity descriptor has a larger value in polar solvents than in nonpolar solvents. Furthermore, an analysis of these results shows that atoms N4 and C25 have the highest values of f_k^+, suggesting that these sites act as electron acceptors. On the other hand, atoms O2 and C5 have large values of f_k^-, indicating that they act as electron donors. The local philicity index and dual descriptor $\Delta f(r)$ (see Fig. S6) exhibit a remarkable agreement with the FF, and it is found that atom C5 is the preferred site for electrophilic attack.

3.5.3. TD–DFT calculations of absorption spectra. The electronic spectral analysis of the title compound was performed using the time-dependent DFT (TD–DFT) method

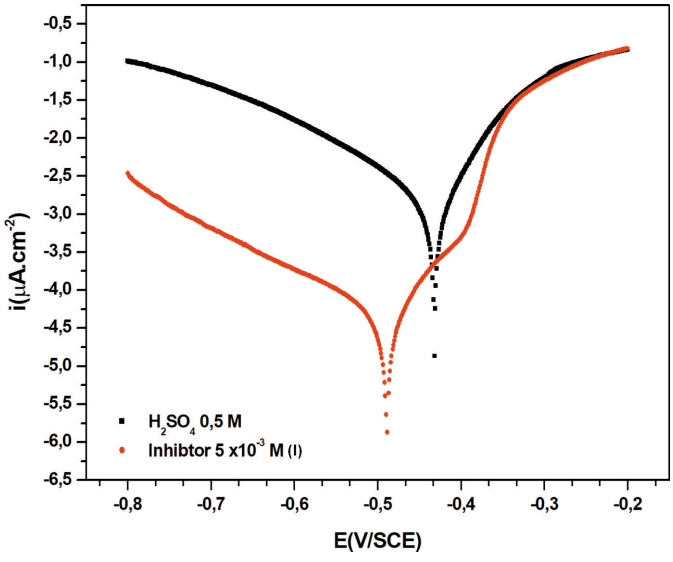

Figure 6
Polarization curves for steel in 0.5 *M* H_2SO_4 solution with and without 5×10^{-3} *M* of inhibitor **I** at 298 K.

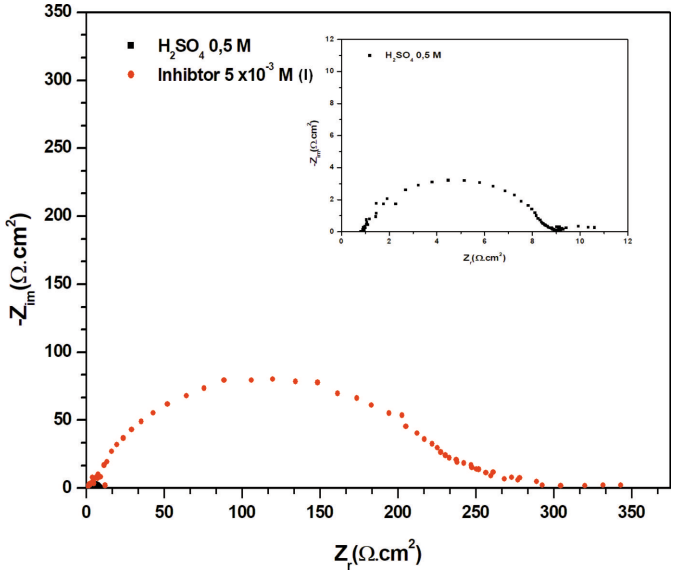

Figure 7
EIS for mild steel in 0.5 *M* H_2SO_4 solution with and without 5×10^{-3} *M* of inhibitor **I** at 298 K.

Table 7
Local reactivity descriptors calculated for the corrosion inhibitor **I** in the gas phase and in various solvents [values in parentheses represent $\Delta f(r) > 0$ and $\Delta f(r) < 0$].

	Gas		*n*-Hexane		Chloroform		DCM		Acetone		Methanol		Water	
	f^-	Δf	f^-	Δf	f^-	Δf	f^-	Δf	f^-	Δf	f^-	Δf	f^-	Δf
O1	0.0443	−0.0204	0.0447	−0.0199	0.0484	−0.0236	0.0532	−0.0285	0.0579	−0.0334	0.0594	−0.035	0.0609	−0.0365
O2	0.0754	−0.0469	0.0697	−0.0449	0.0589	−0.037	0.0501	−0.0291	0.0424	−0.022	0.0401	−0.0199	0.0379	−0.0179
N4	0.0353	0.0859	0.0485	0.0781	0.0652	0.0672	0.075	0.0598	0.0821	0.0544	0.084	0.0529	0.0856	0.0518
C5	0.0624	−0.0487	0.073	−0.0597	0.0938	(−0.0816)	0.1119	−0.1001	0.1284	(−0.117)	0.1344	−0.1242	0.1392	−0.1292
C25	0.0116	0.0977	0.0084	0.1178	−0.0009	0.1416	−0.01	0.1387	−0.018	(0.135)	−0.0199	0.134	−0.0221	0.1332
C27	0.0613	−0.0242	0.0588	−0.027	0.048	−0.021	0.0364	−0.0113	0.0258	−0.0019	0.0228	0.0008	0.0199	0.0033

and the IEFPCM model in gas and various polar and nonpolar solvent phases. The calculations were carried out at the TD-M062x/6-311+g(d) level of theory on the ground-state-optimized geometry. The computed absorption spectrum, wavelength (nm), excitation energy (eV) and oscillator strengths (f_{os}), as well as the absorption properties of compound **I**, are presented in Table 7 and Figs. S3 and S4 of the supporting information.

The simulated UV–Vis spectrum of **I** (Fig. S7) contains two regions of high oscillator strengths falling in the ranges 180–280 and 280–450 nm. From the TD–DFT outcomes it is apparent that the solvent does not have a significant impact on the UV–Vis spectrum. Conversely, when comparing the computed and experimental spectra, a shift towards higher wavelength can be observed for the experimental results, and the discrepancy between them is minimal. On the other hand, we can observe that the most intense band centred at about 351 and 345 nm (f = 0.8 and 0.6) for the solvent and gas phases, respectively, is caused by a HOMO→LUMO electronic transition (see Table 7). Analysis of the frontier orbitals (Fig. S8) shows that this transition has a mixed character of $\pi\rightarrow\pi^*$ and n→π^* (n in N and O atoms). Furthermore, a moderate absorption band was observed at ∼231 nm for the solvent and at 226 nm (f = 0.44) in the gas phase, which corresponds to the electronic transition from HOMO-3 to LUMO having a $\pi\rightarrow\pi^*$ character, where π is localized on fragment **I** (see Fig. S3 in the supporting information). The absorption bands observed at 296 nm in acetone and methanol are a result of the HOMO-1→LUMO transitions with n→π^*/$\pi\rightarrow\pi^*$ character, and these transitions exhibit lower oscillator strengths with a value of f = 0.004, whereas the band at 199 nm is due to a HOMO-1→LUMO+2 transition with n→π^*/$\pi\rightarrow\pi^*$ character (where the π^* is localized in fragment **I**).

4. Conclusions

The title Schiff base, (*E*)-2-{[(4-methoxynaphthalen-1-yl)-methylidene]amino}-4-methylphenol (**I**) was synthesized and its structure characterized by X-ray diffraction analysis and by IR, ^{1}H NMR and UV–Vis spectroscopies. All the major interatomic and intermolecular interactions have been discussed and explained. The Hirshfeld surface analysis was carried out and indicated the dominance of the H···H (54.9%) and C···H/H···C (19.1%) interatomic contacts in the crystal lattice, which could be helpful for future drug design. The high chemical hardness and chemical potential as an anticorrosive agent emphasizes the possible use of **I** in the metals industry, and it has been shown to be a promising anticorrosive agent. The results obtained by both methods show that compound **I** could serve as an effective corrosion inhibitor of API 5L Grade B steel in 0.5 *M* H_2SO_4. The corrosion inhibition potentials of **I** were investigated using quantum chemical calculations at the ω B97XD level with the 6-311+g(d) basis set in the gas phase and in various solvents.

Acknowledgements

The authors acknowledge the University of Mentouri Brothers, Constantine 1, for constant support. The authors thank the Institute of Analytical Sciences, University Claude Bernard Lyon 1, France, for use of their computing facilities. HSE is grateful to the University of Neuchâtel for their support over the years. Funding for this research was provided by the Department of Higher Scientific Research and CHEMS Research Unit, University of Constantine 1, CRBT research center, Algeria.

References

Afshari, F., Ghomi, E. R., Dinari, M. & Ramakrishna, S. (2023). *Chem. Select*, **8**, e202203231.
Alaoui Mrani, S., Ech-chihbi, E., Arrousse, N., Rais, Z., El Hajjaji, F., El Abiad, C., Radi, S., Mabrouki, J., Taleb, M. & Jodeh, S. (2021). *Arab. J. Sci. Eng.* **46**, 5691–5707.
Aljourani, J., Raeissi, K. & Golozar, M. A. (2009). *Corros. Sci.* **51**, 1836–1843.
Brown, E. V. & Granneman, G. R. (1975). *J. Am. Chem. Soc.* **97**, 621–627.
Chandra, S., Jain, D., Sharma, A. K. & Sharma, P. (2009). *Molecules*, **14**, 174–190.
Chen, X. M., Li, H. R., Feng, X. L., Wang, H. T. & Sun, X. H. (2022). *ACS Omega*, **7**, 24942–24950.
Deng, S., Li, X. & Fu, H. (2011). *Corros. Sci.* **53**, 3596–3602.
Domingo, L. R., Aurell, M. J., Pérez, P. & Contreras, R. (2002). *Tetrahedron*, **58**, 4417–4423.
Döner, A., Solmaz, R., Özcan, M. & Kardaş, G. (2011). *Corros. Sci.* **53**, 2902–2913.
Fellahi, Z., Chenaf-Ait youcef, H., Hannachi, D., Djedouani, A., Ouksel, L., François, M., Fleutot, S. & Bourzami, R. (2021). *J. Mol. Struct.* **1244**, 130955.
Frisch, M. J., Trucks, G. W., Schlegel, H. B., Scuseria, G. E., Robb, M. A., Cheeseman, J. R., Scalmani, G., Barone, V., Petersson, G. A., Nakatsuji, H., Li, X., Caricato, M., Marenich, A. V., Bloino, J., Janesko, B. G., Gomperts, R., Mennucci, B., Hratchian, H. P., Ortiz, J. V., Izmaylov, A. F., Sonnenberg, J. L., Williams-Young, D., Ding, F., Lipparini, F., Egidi, F., Goings, J., Peng, B., Petrone, A.,

Henderson, T., Ranasinghe, D., Zakrzewski, V. G., Gao, J., Rega, N., Zheng, G., Liang, W., Hada, M., Ehara, M., Toyota, K., Fukuda, R., Hasegawa, J., Ishida, M., Nakajima, T., Honda, Y., Kitao, O., Nakai, H., Vreven, T., Throssell, K., Montgomery, J. A. Jr, Peralta, J. E., Ogliaro, F., Bearpark, M. J., Heyd, J. J., Brothers, E. N., Kudin, K. N., Staroverov, V. N., Keith, T. A., Kobayashi, R., Normand, J., Raghavachari, K., Rendell, A. P., Burant, J. C., Iyengar, S. S., Tomasi, J., Cossi, M., Millam, J. M., Klene, M., Adamo, C., Cammi, R., Ochterski, J. W., Martin, R. L., Morokuma, K., Farkas, O., Foresman, J. B. & Fox, D. J. (2019). *GAUSSIAN16*. Revision C.01. Gaussian Inc., Wallingford, CT, USA. https://gaussian.com/.

Groom, C. R., Bruno, I. J., Lightfoot, M. P. & Ward, S. C. (2016). *Acta Cryst.* B**72**, 171–179.

Hannachi, D., El Houda Amrane, N., Merzoud, L. & Chermette, H. (2021). *New J. Chem.* **45**, 13451–13462.

Hannachi, D., Ouddai, N., Arotçaréna, M. & Chermette, H. (2015). *Mol. Phys.* **113**, 1541–1550.

Jafari, H., Ameri, E., Rezaeivala, M. & Berisha, A. (2022). *J. Indian Chem. Soc.* **99**, 100665.

John, M., Ralls, M. A., Kuruveri, U. B. & Menezes, P. M. (2023). *Metals*, **13**, 397.

Küstü, C., Emregül, K. C. & Atakol, O. (2007). *Corros. Sci.* **49**, 2800–2814.

Lashgari, M., Arshadi, M. R. & Miandari, S. (2010). *Electrochim. Acta*, **55**, 6058–6063.

Lemoui, R., Allal, H., Hannachi, D., Djedouani, A., Ramli, I., Mohamed el hadi, S., Habila, I., Zabat, M., Merazig, H., Stoeckli-Evans, H. & Ghichi, N. (2023). *J. Mol. Struct.* **1286**, 135569.

Lesar, A. & Milošev, I. (2009). *Chem. Phys. Lett.* **483**, 198–203.

Li, C., Yang, W., Zhou, W., Zhang, M., Xue, R., Li, M. & Cheng, Z. (2016). *New J. Chem.* **40**, 8837–8845.

Li, X., Deng, S. & Fu, H. (2011). *Corros. Sci.* **53**, 302–309.

Macrae, C. F., Sovago, I., Cottrell, S. J., Galek, P. T. A., McCabe, P., Pidcock, E., Platings, M., Shields, G. P., Stevens, J. S., Towler, M. & Wood, P. A. (2020). *J. Appl. Cryst.* **53**, 226–235.

Matsumoto, Y., Sawamura, J., Murata, Y., Nishikata, T., Yazaki, R. & Ohshima, T. (2020). *J. Am. Chem. Soc.* **142**, 8498–8505.

McKinnon, J. J., Jayatilaka, D. & Spackman, M. A. (2007). *Chem. Commun.* pp. 3814–3816.

Mezhoud, B., Bouchouit, M., Said, M. E., Messaadia, L., Belfaitah, A., Merazig, H., Chibani, A., Bouacida, S. & Bouraiou, A. (2016). *Res. Chem. Intermed.* **42**, 7451.

Michaelson, H. B. (1977). *J. Appl. Phys.* **48**, 4729–4733.

Mishra, N., Yadav, R., Kumar, K., Pandey, H. & Pandey, R. (2020). *J. Phys. Conf. Ser.* **1504**, 012002.

Mohamed, G. G. (2006). *Spectrochim. Acta A Mol. Biomol. Spectrosc.* **64**, 188–195.

Morell, C., Grand, A. & Toro-Labbé, A. (2005). *J. Phys. Chem. A*, **109**, 205–212.

Musa, A. Y., Kadhum, A. A. H., Mohamad, A. B. & Takriff, M. S. (2010). *Corros. Sci.* **52**, 3331–3340.

Obot, I. B., Obi-Egbedi, N. O. & Umoren, S. A. (2009). *Corros. Sci.* **51**, 276–282.

Olar, R., Badea, M., Ferbinteanu, M., Stanica, N. & Alan, I. (2017). *J. Therm. Anal. Calorim.* **127**, 709–719.

Orona, G., Molinar, V., Fronczek, F. R. & Isovitsch, R. (2011). *Acta Cryst.* E**67**, o2505–o2506.

Parr, R. G. & Pearson, R. G. (1983). *J. Am. Chem. Soc.* **105**, 7512–7516.

Parr, R. G., von Szentpály, L. & Liu, S. (1999). *J. Am. Chem. Soc.* **121**, 1922–1924.

Parr, R. G. & Yang, W. (1984). *J. Am. Chem. Soc.* **106**, 4049–4050.

Qin, W., Long, S., Panunzio, M. & Biondi, S. (2013). *Molecules*, **18**, 12264–12289.

Roy, R. K., Krishnamurti, S., Geerlings, P. & Pal, S. (1998). *J. Phys. Chem. A*, **102**, 3746–3755.

Sakki, B., Said, M. E., Mezhoud, B., Allal, H., Larbah, L., Kherrouba, A., Chibani, A. & Bouraiou, A. (2022). *J. Adh. Sci. Tech.* **36**, 2245–2268.

Segura, J. L., Mancheño, M. J. & Zamora, F. (2016). *Chem. Soc. Rev.* **45**, 5635–5671.

Sheldrick, G. M. (2008). *Acta Cryst.* A**64**, 112–122.

Sheldrick, G. M. (2015). *Acta Cryst.* C**71**, 3–8.

Sk, I., Khan, M. A., Haque, A., Ghosh, S., Roy, D., Homechuadhuri, S. & Alam, M. A. (2020). *Curr. Opin. Green Sustain. Chem.* **3**, 100006.

Spackman, M. A. & Jayatilaka, D. (2009). *CrystEngComm*, **11**, 19–32.

Spackman, P. R., Turner, M. J., McKinnon, J. J., Wolff, S. K., Grimwood, D. J., Jayatilaka, D. & Spackman, M. A. (2021). *J. Appl. Cryst.* **54**, 1006–1011.

Spek, A. L. (2020). *Acta Cryst.* E**76**, 1–11.

Stoe & Cie (2022). *WinXpose*, *Recipe*, *Integrate* and *LANA* in *X-AREA*. Stoe & Cie GmbH, Darmstadt, Germany.

Tan, S. L., Jotani, M. M. & Tiekink, E. R. T. (2019). *Acta Cryst.* E**75**, 308–318.

Tarafder, M. T. H., Ali, M. A., Saravanan, N., Weng, W. Y., Kumar, S., Umar-Tsafe, N. & Crouse, K. A. (2000). *Transition Met. Chem.* **25**, 295–298.

Westrip, S. P. (2010). *J. Appl. Cryst.* **43**, 920–925.

Yakan, H., Omer, H. S., Buruk, O., Çakmak, Ş., Marah, S., Veyisoğlu, A., Muğlu, H., Ozen, T. & Kütük, H. (2023). *J. Mol. Struct.* **1277**, 134799.

Zakerhamidi, M. S., Ghanadzadeh, A. & Moghadam, M. (2012). *Chem. Sci. Trans.* **1**, 1–8.

Zhang, Z., Song, Q., Jin, Y., Feng, Y., Li, J. & Zhang, K. (2023). *Metals*, **13**, 386.

Zheludkevich, M. L., Yasakau, K. A., Poznyak, S. K. & Ferreira, M. G. S. (2005). *Corros. Sci.* **47**, 3368–3383.

supporting information

Acta Cryst. (2023). C**79**, 324-333 [https://doi.org/10.1107/S2053229623005867]

The synthesis and crystal structure of (*E*)-2-{[(4-methoxynaphthalen-1-yl)methylidene]amino}-4-methylphenol: Hirshfeld surface analysis, DFT calculations and anticorrosion studies

Ahmed Abderrahim Yahiaoui, Nadir Ghichi, Douniazed Hannachi, Bilel Mezhoud, Amel Djedouani, Khairedine Kraim, Aurélien Crochet and Helen Stoeckli-Evans

Computing details

Data collection: WinXpose in *X-AREA* (Stoe & Cie, 2022); cell refinement: Recipe in *X-AREA* (Stoe & Cie, 2022); data reduction: Integrate and LANA in *X-AREA* (Stoe & Cie, 2022); program(s) used to solve structure: *SHELXS97* (Sheldrick, 2008); program(s) used to refine structure: *SHELXL2018* (Sheldrick, 2015); molecular graphics: *PLATON* (Spek, 2020) and *Mercury* (Macrae *et al.*, 2020); software used to prepare material for publication: *SHELXL2018* (Sheldrick, 2015), *PLATON* (Spek, 2020) and *publCIF* (Westrip, 2010).

(*E*)-2-{[(4-Methoxynaphthalen-1-yl)methylidene]amino}-4-methylphenol

Crystal data

$C_{19}H_{17}NO_2$
M_r = 291.33
Triclinic, $P\overline{1}$
a = 7.7740 (4) Å
b = 7.9955 (4) Å
c = 12.4836 (6) Å
α = 106.383 (4)°
β = 98.191 (4)°
γ = 93.279 (4)°
V = 732.96 (7) Å^3
Z = 2
$F(000)$ = 308
D_x = 1.320 Mg m^{-3}
Mo $K\alpha$ radiation, λ = 0.71073 Å
Cell parameters from 11095 reflections
θ = 1.7–27.3°
μ = 0.09 mm^{-1}
T = 250 K
Block, orange
0.61 × 0.39 × 0.18 mm

Data collection

STOE IPDS II diffractometer
Radiation source: sealed X-ray tube, 12 x 0.4 mm long-fine focus
Plane graphite monochromator
Detector resolution: 6.67 pixels mm^{-1}
rotation method, ω scans
Absorption correction: multi-scan (MULABS; Spek, 2020)
T_{min} = 0.875, T_{max} = 1.000
11018 measured reflections
3090 independent reflections
2742 reflections with $I > 2\sigma(I)$
R_{int} = 0.018
θ_{max} = 26.8°, θ_{min} = 1.7°
h = −9→9
k = −10→9
l = −15→15

Refinement

Refinement on F^2
Least-squares matrix: full
$R[F^2 > 2\sigma(F^2)] = 0.038$
$wR(F^2) = 0.113$
$S = 1.04$
3090 reflections
205 parameters
0 restraints
Primary atom site location: structure-invariant direct methods
Secondary atom site location: difference Fourier map
Hydrogen site location: mixed
H atoms treated by a mixture of independent and constrained refinement
$w = 1/[\sigma^2(F_o^2) + (0.0629P)^2 + 0.1103P]$ where $P = (F_o^2 + 2F_c^2)/3$
$(\Delta/\sigma)_{max} = 0.005$
$\Delta\rho_{max} = 0.20$ e Å^{-3}
$\Delta\rho_{min} = -0.14$ e Å^{-3}

Special details

Geometry. All esds (except the esd in the dihedral angle between two l.s. planes) are estimated using the full covariance matrix. The cell esds are taken into account individually in the estimation of esds in distances, angles and torsion angles; correlations between esds in cell parameters are only used when they are defined by crystal symmetry. An approximate (isotropic) treatment of cell esds is used for estimating esds involving l.s. planes.

Fractional atomic coordinates and isotropic or equivalent isotropic displacement parameters (Å^2)

	x	*y*	*z*	U_{iso}*/U_{eq}
O1	0.37640 (11)	0.70357 (10)	0.74315 (6)	0.0478 (2)
O2	0.00186 (12)	0.95474 (11)	0.15984 (8)	0.0533 (2)
H2O	0.031 (2)	0.935 (2)	0.2219 (16)	0.084 (6)*
N1	−0.00350 (12)	0.69499 (12)	0.25196 (8)	0.0417 (2)
C1	0.13306 (13)	0.60555 (14)	0.40839 (9)	0.0361 (2)
C2	0.13789 (14)	0.76848 (14)	0.48464 (9)	0.0402 (2)
H2	0.085081	0.856781	0.459797	0.048*
C3	0.21806 (15)	0.80813 (14)	0.59750 (9)	0.0415 (2)
H3	0.219226	0.921233	0.647190	0.050*
C4	0.29521 (13)	0.68039 (14)	0.63528 (9)	0.0379 (2)
C5	0.37175 (15)	0.37629 (15)	0.59984 (10)	0.0431 (3)
H5	0.423752	0.401751	0.676141	0.052*
C6	0.37224 (16)	0.21274 (15)	0.52838 (11)	0.0478 (3)
H6	0.423091	0.125544	0.555505	0.057*
C7	0.29682 (16)	0.17444 (14)	0.41423 (10)	0.0465 (3)
H7	0.299056	0.061774	0.364824	0.056*
C8	0.22010 (14)	0.29895 (14)	0.37397 (9)	0.0413 (2)
H8	0.170368	0.270557	0.297080	0.050*
C9	0.21401 (12)	0.47005 (13)	0.44580 (8)	0.0349 (2)
C10	0.29405 (13)	0.50852 (13)	0.56089 (9)	0.0360 (2)
C11	0.3970 (2)	0.87468 (17)	0.81915 (11)	0.0625 (4)
H11C	0.463971	0.874752	0.890943	0.094*
H11B	0.283063	0.912636	0.830827	0.094*
H11A	0.458215	0.954118	0.787835	0.094*
C12	0.04229 (13)	0.57172 (14)	0.29245 (9)	0.0387 (2)
H12	0.016817	0.455204	0.246166	0.046*
C13	−0.09569 (13)	0.65748 (14)	0.14067 (9)	0.0383 (2)
C14	−0.18898 (14)	0.49935 (14)	0.07476 (9)	0.0414 (3)

H14	−0.194706	0.404229	0.104854	0.050*
C15	−0.27369 (14)	0.47931 (15)	−0.03449 (9)	0.0414 (3)
C16	−0.26515 (15)	0.62281 (16)	−0.07652 (9)	0.0447 (3)
H16	−0.322371	0.611432	−0.150197	0.054*
C17	−0.17448 (16)	0.78190 (15)	−0.01252 (10)	0.0459 (3)
H17	−0.170458	0.877361	−0.042377	0.055*
C18	−0.09002 (14)	0.79882 (14)	0.09561 (9)	0.0407 (2)
C19	−0.37175 (17)	0.30697 (16)	−0.10504 (10)	0.0523 (3)
H19A	−0.495364	0.310829	−0.101543	0.078*
H19B	−0.329154	0.213780	−0.076131	0.078*
H19C	−0.354011	0.285087	−0.182962	0.078*

Atomic displacement parameters (Å²)

	U^{11}	U^{22}	U^{33}	U^{12}	U^{13}	U^{23}
O1	0.0577 (5)	0.0459 (4)	0.0346 (4)	0.0057 (4)	−0.0041 (3)	0.0091 (3)
O2	0.0640 (6)	0.0426 (5)	0.0495 (5)	−0.0021 (4)	−0.0053 (4)	0.0161 (4)
N1	0.0428 (5)	0.0459 (5)	0.0368 (5)	0.0026 (4)	0.0009 (4)	0.0157 (4)
C1	0.0341 (5)	0.0402 (5)	0.0353 (5)	0.0018 (4)	0.0042 (4)	0.0143 (4)
C2	0.0427 (6)	0.0391 (5)	0.0410 (6)	0.0070 (4)	0.0045 (4)	0.0158 (4)
C3	0.0470 (6)	0.0367 (5)	0.0388 (5)	0.0047 (4)	0.0051 (4)	0.0088 (4)
C4	0.0370 (5)	0.0415 (5)	0.0340 (5)	0.0002 (4)	0.0022 (4)	0.0118 (4)
C5	0.0430 (6)	0.0456 (6)	0.0419 (6)	0.0045 (5)	0.0002 (4)	0.0180 (5)
C6	0.0490 (6)	0.0416 (6)	0.0560 (7)	0.0091 (5)	0.0039 (5)	0.0211 (5)
C7	0.0507 (6)	0.0353 (5)	0.0511 (6)	0.0053 (5)	0.0068 (5)	0.0096 (5)
C8	0.0428 (6)	0.0405 (5)	0.0386 (5)	0.0012 (4)	0.0037 (4)	0.0106 (4)
C9	0.0322 (5)	0.0364 (5)	0.0368 (5)	0.0004 (4)	0.0049 (4)	0.0130 (4)
C10	0.0330 (5)	0.0379 (5)	0.0373 (5)	0.0005 (4)	0.0037 (4)	0.0131 (4)
C11	0.0786 (9)	0.0528 (7)	0.0423 (6)	0.0112 (6)	−0.0096 (6)	0.0007 (5)
C12	0.0374 (5)	0.0426 (6)	0.0364 (5)	0.0039 (4)	0.0041 (4)	0.0130 (4)
C13	0.0369 (5)	0.0440 (6)	0.0350 (5)	0.0064 (4)	0.0037 (4)	0.0142 (4)
C14	0.0411 (6)	0.0429 (6)	0.0415 (6)	0.0040 (4)	0.0030 (4)	0.0165 (4)
C15	0.0377 (5)	0.0460 (6)	0.0393 (5)	0.0068 (4)	0.0044 (4)	0.0108 (4)
C16	0.0452 (6)	0.0546 (7)	0.0345 (5)	0.0108 (5)	0.0021 (4)	0.0146 (5)
C17	0.0519 (6)	0.0470 (6)	0.0435 (6)	0.0098 (5)	0.0046 (5)	0.0214 (5)
C18	0.0413 (5)	0.0402 (5)	0.0408 (6)	0.0060 (4)	0.0041 (4)	0.0133 (4)
C19	0.0507 (7)	0.0514 (7)	0.0477 (6)	0.0010 (5)	−0.0011 (5)	0.0087 (5)

Geometric parameters (Å, º)

O1—C4	1.3601 (12)	C8—C9	1.4161 (15)
O1—C11	1.4131 (14)	C8—H8	0.9400
O2—C18	1.3705 (14)	C9—C10	1.4212 (14)
O2—H2O	0.835 (18)	C11—H11C	0.9700
N1—C12	1.2741 (14)	C11—H11B	0.9700
N1—C13	1.4109 (13)	C11—H11A	0.9700
C1—C2	1.3745 (15)	C12—H12	0.9400
C1—C9	1.4379 (14)	C13—C14	1.3927 (15)

C1—C12	1.4603 (14)	C13—C18	1.3983 (15)
C2—C3	1.3961 (15)	C14—C15	1.3886 (15)
C2—H2	0.9400	C14—H14	0.9400
C3—C4	1.3735 (15)	C15—C16	1.3917 (16)
C3—H3	0.9400	C15—C19	1.5031 (16)
C4—C10	1.4238 (15)	C16—C17	1.3845 (16)
C5—C6	1.3599 (17)	C16—H16	0.9400
C5—C10	1.4137 (15)	C17—C18	1.3805 (15)
C5—H5	0.9400	C17—H17	0.9400
C6—C7	1.4012 (16)	C19—H19A	0.9700
C6—H6	0.9400	C19—H19B	0.9700
C7—C8	1.3653 (16)	C19—H19C	0.9700
C7—H7	0.9400		

C4—O1—C11	117.78 (9)	O1—C11—H11C	109.5
C18—O2—H2O	102.0 (12)	O1—C11—H11B	109.5
C12—N1—C13	120.69 (9)	H11C—C11—H11B	109.5
C2—C1—C9	118.94 (9)	O1—C11—H11A	109.5
C2—C1—C12	119.73 (9)	H11C—C11—H11A	109.5
C9—C1—C12	121.31 (9)	H11B—C11—H11A	109.5
C1—C2—C3	122.66 (10)	N1—C12—C1	122.15 (10)
C1—C2—H2	118.7	N1—C12—H12	118.9
C3—C2—H2	118.7	C1—C12—H12	118.9
C4—C3—C2	119.40 (10)	C14—C13—C18	118.84 (10)
C4—C3—H3	120.3	C14—C13—N1	127.09 (9)
C2—C3—H3	120.3	C18—C13—N1	114.07 (9)
O1—C4—C3	124.60 (10)	C15—C14—C13	121.35 (10)
O1—C4—C10	114.58 (9)	C15—C14—H14	119.3
C3—C4—C10	120.82 (9)	C13—C14—H14	119.3
C6—C5—C10	120.86 (10)	C14—C15—C16	118.20 (10)
C6—C5—H5	119.6	C14—C15—C19	120.66 (10)
C10—C5—H5	119.6	C16—C15—C19	121.14 (10)
C5—C6—C7	119.88 (10)	C17—C16—C15	121.64 (10)
C5—C6—H6	120.1	C17—C16—H16	119.2
C7—C6—H6	120.1	C15—C16—H16	119.2
C8—C7—C6	120.73 (10)	C18—C17—C16	119.29 (10)
C8—C7—H7	119.6	C18—C17—H17	120.4
C6—C7—H7	119.6	C16—C17—H17	120.4
C7—C8—C9	121.27 (10)	O2—C18—C17	120.14 (10)
C7—C8—H8	119.4	O2—C18—C13	119.18 (10)
C9—C8—H8	119.4	C17—C18—C13	120.67 (10)
C8—C9—C10	117.52 (9)	C15—C19—H19A	109.5
C8—C9—C1	123.66 (9)	C15—C19—H19B	109.5
C10—C9—C1	118.82 (9)	H19A—C19—H19B	109.5
C5—C10—C9	119.71 (10)	C15—C19—H19C	109.5
C5—C10—C4	120.94 (10)	H19A—C19—H19C	109.5
C9—C10—C4	119.35 (9)	H19B—C19—H19C	109.5

C9—C1—C2—C3	−0.17 (16)	O1—C4—C10—C5	0.35 (15)
C12—C1—C2—C3	178.14 (9)	C3—C4—C10—C5	−179.33 (10)
C1—C2—C3—C4	−0.26 (17)	O1—C4—C10—C9	−179.44 (8)
C11—O1—C4—C3	−6.08 (17)	C3—C4—C10—C9	0.89 (16)
C11—O1—C4—C10	174.26 (11)	C13—N1—C12—C1	−178.08 (9)
C2—C3—C4—O1	−179.75 (10)	C2—C1—C12—N1	14.20 (16)
C2—C3—C4—C10	−0.11 (17)	C9—C1—C12—N1	−167.54 (10)
C10—C5—C6—C7	0.76 (18)	C12—N1—C13—C14	19.32 (17)
C5—C6—C7—C8	−1.01 (18)	C12—N1—C13—C18	−161.18 (10)
C6—C7—C8—C9	−0.06 (18)	C18—C13—C14—C15	0.86 (16)
C7—C8—C9—C10	1.32 (16)	N1—C13—C14—C15	−179.66 (10)
C7—C8—C9—C1	−179.17 (10)	C13—C14—C15—C16	−0.84 (16)
C2—C1—C9—C8	−178.57 (10)	C13—C14—C15—C19	179.16 (10)
C12—C1—C9—C8	3.15 (16)	C14—C15—C16—C17	0.33 (17)
C2—C1—C9—C10	0.94 (15)	C19—C15—C16—C17	−179.66 (11)
C12—C1—C9—C10	−177.34 (9)	C15—C16—C17—C18	0.14 (18)
C6—C5—C10—C9	0.53 (17)	C16—C17—C18—O2	179.35 (10)
C6—C5—C10—C4	−179.26 (10)	C16—C17—C18—C13	−0.12 (17)
C8—C9—C10—C5	−1.54 (15)	C14—C13—C18—O2	−179.84 (10)
C1—C9—C10—C5	178.92 (9)	N1—C13—C18—O2	0.61 (15)
C8—C9—C10—C4	178.25 (9)	C14—C13—C18—C17	−0.37 (17)
C1—C9—C10—C4	−1.29 (14)	N1—C13—C18—C17	−179.92 (10)

Hydrogen-bond geometry (Å, º)

Cg1 is the centroid of the phenol ring, C13-C18.

D—H···*A*	*D*—H	H···*A*	*D*···*A*	*D*—H···*A*
O2—H2*O*···N1	0.84 (2)	2.069 (18)	2.6436 (13)	126 (2)
C11—H11*B*···O2^{i}	0.97	2.51	3.4725 (19)	170
C19—H19*A*···*Cg*1^{ii}	0.97	2.79	3.7362 (14)	165

Symmetry codes: (i) −*x*, −*y*+2, −*z*+1; (ii) −*x*−1, −*y*+1, −*z*.